Research Article Vol. 32, No. 25 / 2 Dec 2024 / Optics Express 44115

Optics EXPRESS

DC-stable electro-optic modulators using thin-film lithium tantalate

KEITH POWELL, XUDONG LI, DANIEL ASSUMPCAO, LETÍCIA MAGALHÃES, NEIL SINCLAIR, AND MARKO LONČAR*

John A. Paulson School of Engineering and Applied Sciences, Harvard University, Cambridge, Massachusetts 02138, USA
*loncar@seas.harvard.edu

Abstract: We demonstrate telecommunication-wavelength Pockels electro-optic modulators in thin-film lithium tantalate (TFLT) with superior DC stability compared to equivalent thin-film lithium niobate (TFLN) modulators. Less than 1 dB output power fluctuation for quadrature-biased TFLT is measured compared to 5 dB with TFLN over 46 hours with 12.1 dBm input power. Our TFLT modulators maintain properties similar to those in TFLN: 3.4 Vcm half-wave voltage length product, 39 dB extinction ratio, flat RF electro-optic response from 3-50 GHz, and 0.35 dB on-chip loss. We also show low error-rate data modulation over 0-70°C with TFLT modulators and optical loss of 9 dB/m.

1. Introduction

Thin-film lithium niobate (TFLN) integrated electro-optic (EO) circuits have bolstered many advancements in optical science and technology over the last several years [1]. The most seminal EO device–the Mach-Zehnder modulator (MZM)– benefits a host of technologies in optical communications, sensing and computing. TFLN MZMs at telecommunication wavelengths have shown low half-wave voltage length products ($V_\pi L$), e.g., 2.3 Vcm, and EO bandwidths beyond 100 GHz [1]. Optical loss of TFLN was recently measured to be as low as 1.3 dB/m [2]. An unresolved issue with TFLN modulators is slow (<kHz) relaxation of the EO response. As a result, active EO control of the modulator is employed, or alternatively thermo-optic based control and biasing is utilized to maintain bias point [3,4] . The former, however, introduces additional complexities related to the stability of the low-frequency EO response, while the latter results in increased steady-state power consumption, thermal cross talk and is not compatible with cryogenic operation. Furthermore, at elevated optical powers the photorefractive effect in TFLN can introduce additional relaxation dynamics and instabilities, that can be exacerbated in thin films, and thus many demonstrations use low input power and/or power-consuming amplifiers at the chip output to compensate this effect [1].

Lithium tantalate (LT) is known to have slower and a smaller magnitude of EO relaxation than LN, while featuring comparable, or better, properties [5–8]: EO coefficient (r_{33}~30 pm/V) [9], bandgap 3.93 eV [10], 23× lower birefringence than LN at 633 nm [11], 5× lower photorefraction than LN at visible wavelengths [12,13], 2500× higher optical damage threshold than LN for green light [5,14], and 10× lower RF loss tangent than LN [11,15]. Yet, optical modulators using waveguides in bulk LT have not been as widely adopted as those in LN [16], whereas LT and TFLT have had extensive use in acoustic filters [17]. This is partially due the low Curie temperature of LT, which restricts the creation of low-loss optical waveguides in LT via doping or ion exchange, in combination with instability issues [16]. Recently, the first optical devices on TFLT have appeared: microdisks [5], strip-loaded waveguides [6], as well as dry-etched microrings [7], and MZMs [8]. Nevertheless, it is still unclear as to what extent the desirable properties of bulk LT map to thin-film LT electro-optic modulators, e.g., weak EO relaxation, without sacrificing other metrics such as drive voltage, optical loss, and so on.

#538870 https://doi.org/10.1364/OE.538870
Journal © 2024 Received 16 Aug 2024; revised 1 Nov 2024; accepted 4 Nov 2024; published 19 Nov 2024

We design, fabricate, and demonstrate TFLT EO MZMs operating at 1550 nm with superior DC stability, in both amplitude and timescale, compared to equivalent TFLN MZMs. Specifically, we measure less than 1 dB output power fluctuation for quadrature-biased TFLT compared to 5 dB with TFLN over 46 hours with 12.1 dBm input power. Importantly, our TFLT MZMs do not sacrifice important device figures-of-merit including optical loss (0.35 dB), RF bandwidth (flat from 3-50 GHz), extinction ratio (39 dB), and drive voltage (3.4 Vcm half-wave voltage), compared to TFLT MZMs. Benefiting from the DC stability, we designed a path-length balanced modulator, which is insensitive to temperature fluctuations. This is demonstrated by measured bit error rates below soft-division forward error correction threshold over a temperature range from 0°C to 70°C. We also measure open eye diagrams for 30 GBaud non-return-to-zero pseudorandom bit sequence modulation using high 28 dBm optical power. Furthermore, to validate the quality of our etch process, we fabricate TFLT racetrack resonators and measure low single-mode optical loss of 9 dB/m, and measure a thermo-optic coefficient of TFLT ($dn/dT = 3 \times 10^{-6} K^{-1}$).

2. Fabrication

An optical microscope image of the fabricated TFLT MZM is shown in Fig. 1(a). The device is fabricated on 500 nm-thick x-cut TFLT-on-SiO_2 wafer from NanoLN. The SiO_2 layer is 2 μm-thick and is thermally grown on a Si handle. Waveguides are patterned using ma-N 2405 resist and 150 keV electron-beam lithography (Fig. 1(b)(i)), then etched by 300 nm using Ar^+ inductively coupled plasma dry etching (Fig. 1(b)(ii)). Re-deposition from the etch and removal of the remaining maN-2405 is achieved using KOH and SC-1 solutions each heated to 65 °C. The devices are annealed in an O_2 atmosphere at 520°C for 2 h to restore damage

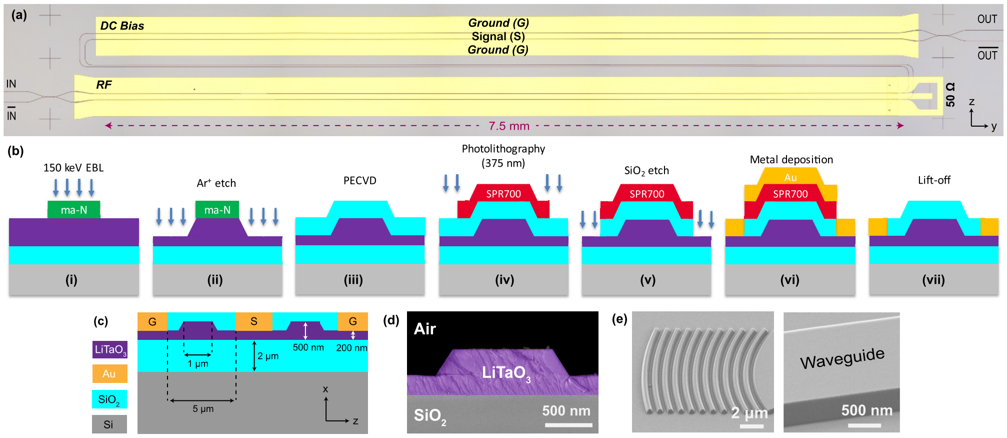

Fig. 1. Integrated thin-film lithium tantalate-on-insulator electro-optics. (a) Micrograph of a balanced Mach-Zehnder modulator with independent DC and 50 Ohm-terminated RF electrodes. (b) Device fabrication process. (i) x-cut thin-film lithium tantalate is coated with ma-N 2405 resist and exposed using 150 kV electro-beam lithography (EBL), (ii) Ar^+ etch defines the waveguides, (iii) plasma-enhanced chemical vapor deposition (PECVD) of an SiO_2 cladding layer, (iv) electrode mask is defined using 375 nm-photolithography and SPR700-1.0 resist, (v) the SiO_2 cladding is selectively removed using inductively coupled plasma etching, (vi) metal deposition of Ti/Au electrodes is performed by electron-beam evaporation, (vii) lift-off is used to define electrodes. (c) Mach-Zehnder modulator cross-section schematic with crystal axes, relevant dimensions, and materials noted. (d) Scanning electron-micrograph (SEM) of a cross section of an etched lithium tantalate waveguide. A sidewall angle of 61° is observed. (e) SEMs of fabricated grating couplers and waveguides showing smooth sidewalls.

in the crystal, thus reducing optical loss and photo-refractive effects. The MZMs are left uncladded to measure the DC electro-optic drift without effects of oxide impurities, so as to fairly compare TFLT crystal properties to TFLN. For high frequency electro-optic measurements and optical resonator measurements, an 800 nm-thick SiO_2 cladding layer is subsequently deposited by plasma-enhanced chemical vapor deposition (Fig. 1(b)(iii)). This reduces the effects of sidewall scattering due to high index contrast between TFLT and air for loss characterization and achieve optimal RF phase and optical group velocity matching. Electrodes are patterned by photolithography at 375 nm with SPR700-1.0 resist (Fig. 1(b)(iv)). Next, for the cladded devices, trenches are dry etched using C_3F_8 and Ar^+ gases (Fig. 1(b)(v)). Metal is deposited using electron-beam evaporation (Fig. 1(b)(vi)). Lift-off defines the MZM electrodes (Fig. 1(b)(vii)) which consist of a 15 nm-thick Ti adhesion layer and 800 nm-thick Au. The termination resistor (20 nm-thick Ti, 5 nm-thick Pt) for the MZM is defined by another round of photolithography, etching, electron-beam deposition, and liftoff. Electrodes for uncladded MZMs are also similarly defined by photolithography, electron-beam deposition, and liftoff. As a final step, all devices are hotplate-heated at 300°C for 5 h to remove trapped charges induced by the electron-beam metal deposition which can negatively impact DC drift effects [18]. To unambiguously compare the DC drift of the TFLT MZM with a TFLN MZM, we fabricate a TFLN MZM using the same process, and with the same waveguide and electrode geometries.

3. Modulator simulations

The optical mode supported by the waveguide fabricated in the 500 nm TFLT-on-2 μm oxide stack, is shown in Fig. 2(a), and features an effective index of 1.9 and group index of 2.25. Next, we perform a microwave simulation with electrodes to check the overlap between optical and microwave electric fields for the 300 nm etch depth we use. As shown in Fig. 2(b), most of the microwave field in the surrounding oxide and slab due to the high permittivity contrast between lithium tantalate (~43) and SiO_2 (~4) at these frequencies. By using the same mesh in the waveguide region for both optical and RF simulations, we obtain an accurate field overlap over an entire cross- section and estimate the DC $V_\pi L$ by calculating the RF-induced index change of optical mode. With this process, along with considerations for metal-induced optical loss and fabrication alignment accuracy, the gap between electrodes is chosen to be 5 μm, giving a simulated DC $V_\pi L$ of 3.1 Vcm.

To achieve high-bandwidth performance of the modulator, we first address the required matching of optical group velocity to microwave phase velocity at high frequencies [1]. Given our stack, matching is achieved by choosing the correct width for signal electrode (Fig. 2(c)), which is 50 μm. Next we address matching the impedance of the modulator, which is essentially a co-planar transmission line in ground-signal-ground configuration, to the 50Ω RF loading port. Unfortunately, we find that with the current stack and limiting tuning parameters, the best impedance we can achieve while maintaining velocity matching is 39Ω (Fig. 2(d)). This was inferred from our measurements of the electro-optic response of the modulator shown in Sec. 6. We expect this will lead to a sharp roll-off at frequencies from hundreds of megahertz to a few gigahertz where the electrical modulation speed enters RF regime and reflections begin to happen. This problem can be alleviated by increasing the thickness of the bottom oxide from the current 2 μm to at least 4.7 μm. It is also worth noting that a segmented electrode design [19] can help increase the impedance, but it will strongly raise the RF index (to above 3 with our stack). Future work on combining the segmented design with thicker bottom oxide will overcome this problem and further improve the bandwidth. Note that independent ellipsometry measurements were used to determine the refractive indices of TFLT, $n_e \sim n_o \sim 2.12$ at 1550 nm, for our simulations and calculations.

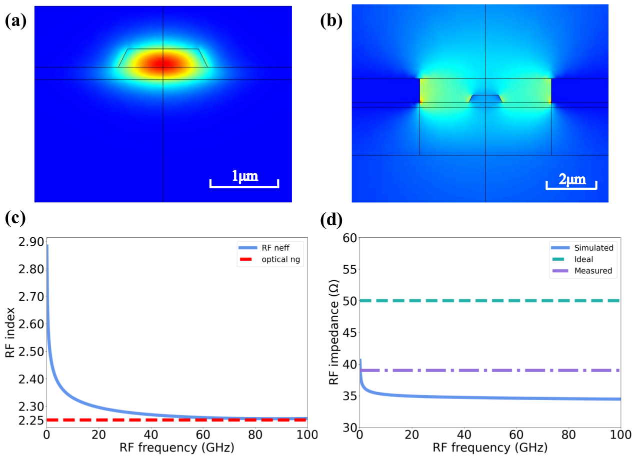

Fig. 2. Simulation for our TFLT modulators. (a) Simulated optical electric field profile (Comsol). The group velocity of the fundamental TE mode (shown) is 2.25. (b) Simulated RF electric field profile (Comsol). The field overlap is calculated and $V_{\pi}L$ at DC is estimated to be 3.1 Vcm. Lines are used to define material boundaries and to guide the eye. (c) Simulated RF effective index "neff" (Lumerical HFSS). By design it matches the group index of light "optical ng" at high frequency. (d) Simulated (Lumerical HFSS), Ideal (50 Ω) and Measured (inferred from electro-optic measurements, 39 Ω) RF impedance.

4. Modulator chip details

We use a path length-balanced MZM to mitigate temperature and laser wavelength fluctuations. Our design is based on directional couplers instead of Y-splitters and hence has two input and two output ports. Separate 7.5 mm-long ground-signal-ground DC and 50 Ω-terminated RF electrodes avoids an external bias-tee, thereby providing excellent isolation between DC and RF signals while enabling low RF insertion loss, flat RF response, and avoids terminator damage under high DC bias. The MZM cross-section (Fig. 1(c) schematic) is optimized for low optical loss with strong optical and RF field overlap. A scanning-electron microscope cross-section of the etched waveguide (Fig. 1(d)) is used to determine the etched sidewall angle of 61° which is limited by the etch bias power and rate of re-deposition. The sidewall angle is used to design and simulate grating couplers. We measure a loss of 7.9 dB per grating coupler for coupling light between optical fibers and the chips. This differs from the simulated efficiency of ~3 dB due to fabrication imperfections. Figure 1(e) shows a scanning-electron microscope image of the etched grating couplers and waveguides, indicating successful removal of re-deposition and low sidewall roughness.

5. DC electro-optic measurements

We measure low $V_{\pi}L$ of 3.4 Vcm at near-DC (Fig. 3(a)), which is close to that predicted by simulation. The $V_{\pi}L$ is measured by monitoring the output power of each MZM port and slowly varying the input voltage, which matches our simulation and is limited mainly by our current device geometry, including gap width, etch depth, etc. Future work with optimized stack and design would achieve a lower $V_{\pi}L$. Notably, an exceptionally high extinction ratio of 39 dB is measured at one of the ports. The second port has a lower extinction ratio of 16 dB due to asymmetric directional couplers (53:47 ratio) as well as etch-induced error and, as observed using a microscope, loss difference between the two arms induced by misalignment of the electrode (0.7 dB). The above effects of the directional coupler ratio and electrode-induced loss are estimated using simulation. Scattering in the MZM waveguides accounts for 0.13 dB loss, with the metal loss together leading to a total on-chip loss of 0.35 dB. Next, the TFLT MZM is biased at quadrature and EO relaxation is measured over 46 hours using 20 dBm off- (12.1 dBm on-) chip input optical power (Fig. 3(b)). We find <1 dB of laser intensity variation in the first two hours, likely due to charge migration at the electrical contact, settling to 0.2 dB drift over the final 44 hours. On the other hand, the TFLN MZM exhibited 5 dB laser intensity variation when measured under the same conditions, that is, input power and measurement duration. Furthermore, EO relaxation of TFLN reported in literature varies from 3 dB in ~15 minutes [4] to 8 dB over ~30 mins [3]. Also note that optical powers unstated in both works. Note that temperature fluctuations of the room (less than 2°C) and mechanical disturbances, including fiber-to-chip coupling drift, are carefully monitored to ensure they do not play a role in our DC drift measurements.

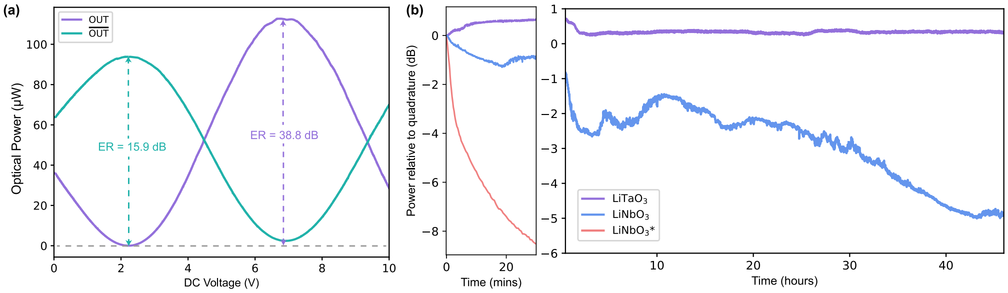

Fig. 3. DC electro-optic characterization measurements. (a) Measured transfer function at each output port of the modulator as a function of slowly varied bias voltage. High extinction ratio of 38.8 dB is measured at output port OUT. A lower extinction ratio of 15.9 dB is measured at the compliment port $\overline{\text{OUT}}$ due fabrication imperfections. (b) Dynamics of optical output intensity relative to quadrature when bias is initially set to quadrature. TFLT (TFLN) MZM exhibits <1dB (5 dB) power drift over 46 hours. First 30 min is shown in left plot. Curve (*) shows the drift of a TFLN MZM from literature [3].

6. RF electro-optic measurements

We measure the RF electro-optic response of our MZM by driving the modulator with a vector network analyzer at quadrature and measuring the variation in output optical power using a high-bandwidth photodiode which is plugged into the second port of the network analyzer. Matching the optical group and RF phase velocities in our modulator design (Fig. 2(c)) produces a normalized electro-optic conversion efficiency (EO S_{21} Fig. 4(a)) with a flat roll-off to 50 GHz after 3 GHz. We were limited to a 50 GHz bandwidth by our spectrum analyzer. The roll-off before 3 GHz is due the low characteristic impedance of the transmission line electrode (39 Ω). As stated in Sec. 3, this can straightforwardly be overcome using an optimized device geometry with a thicker bottom oxide. We also extrapolate the RF EO response using the same methods discussed in Ref. [1], with parameters obtained from simulations (optical and RF indices) and electrical measurements (RF loss and impedance). The result is shown in Fig. 4(a) with dashed line, matching well with experiment. The electrode back-reflection is also monitored with the network analyzer (RF S_{11} Fig. 4(a)). The RF back-reflection is primarily due to the aforementioned RF impedance mismatch, in addition to parasitic resonances.

To show benefit of our stable DC bias in conjunction with our path length-balanced design for data modulation, we bias the MZM at quadrature and drive it using a non-return-to-zero (NRZ) pseudorandom binary sequence (PRBS) at 5 GBaud, over a 70°C temperature range. The temperature is controlled by mounting the chip onto a thermally controlled and monitored

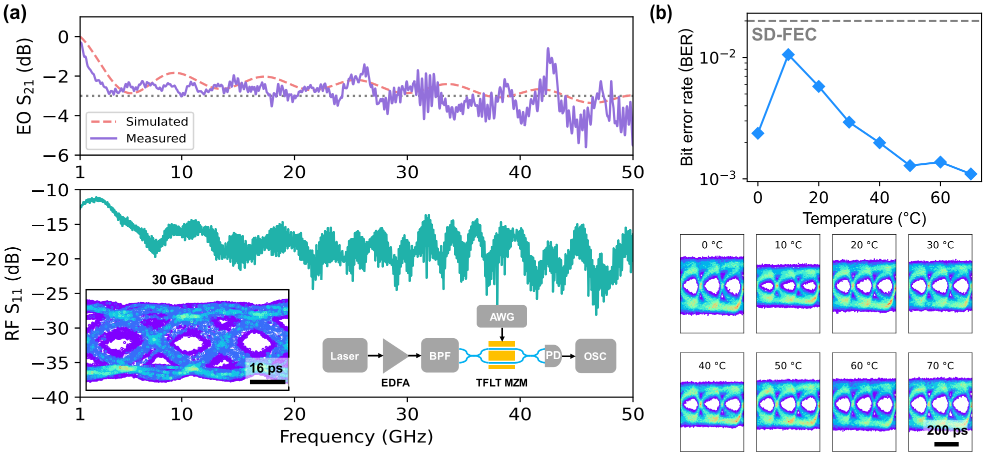

Fig. 4. RF electro-optic characterization measurements. (a) Normalized electro-optic conversion efficiency EO S_{21}, measured (simulated) shown using a solid (dashed) line. The RF S_{11} spectra is shown below. The roll-off before 3 GHz is due the low characteristic impedance of the transmission line electrode (39 Ω), and can be mitigated with thicker underlying oxide and re-optimization of the modulator design. Insets: Eye diagram for 30 GBaud non-return-to-zero pseudorandom bit sequence modulation using high 28 dBm optical power (left) and associated setup (right). EDFA: erbium-doped fiber amplifier, BPF: bandpass filter, AWG: arbitrary waveform generator, PD: photodector, OSC: oscilloscope. (b) Top: Measured bit error rate with 5.1 dBm power is below soft-division forward error correction threshold under varied temperature. Bottom: Eye diagrams at the measured temperatures.

copper stage using clips. Eye diagrams are compiled from 20,000 shots and measured with 5.1 dBm on-chip input optical power (4(b), bottom). All measurements yield bit error rates (BERs) less than that required for soft-division forward error correction (SD-FEC), corresponding to signal-to-noise ratios of ∼3 (Fig. 4(b), top). Above 10°C we measure a reduced error rate with increased temperature. This is due to thermal expansion-induced alignment improvement of the optical fiber with the grating couplers. Increased error is observed at 0°C, owing to misalignment induced by condensation. We expect that proper packaging will reduce the temperature-induced misalignment of the gratings with the fibers.

Finally, at room temperature we increase the on-chip optical power to 28 dBm and demonstrate data modulation (Fig. 4(a), inset). The setup used to perform the measurement is also shown in the inset of Fig. 4(a). We retain open eyes at up to 30 GBaud modulation rates and a signal-to-noise ratio of 3.3, limited by our oscilloscope bandwidth. Instabilities of the optical amplifier prevented accurately testing the long-term DC stability at this power.

7. Optical resonator measurements

For scalability of TFLT, it is pertinent to determine the optical loss induced by our etching process. To estimate this, we fabricate an uncladded racetrack resonator of ∼200 μm width and ∼850 μm in the narrowest and widest parts, respectively. The waveguide was etched by 300 nm, has a 1 μm top width in the coupler section, which corresponds to single mode behavior, and tapers to a maximum 4 μm top width. The bus waveguide has a 1 μm width, which ensures that only the fundamental mode is coupled in and out of the resonator. The gap width between the resonator and the bus is 1.4 μm, corresponding to undercoupled conditions. By varying the wavelength of the laser around 1530 nm, we measure a single-mode spectrum with a free spectral range of 185 pm (Fig. 5(a)). By slowly varying the wavelength of the laser light through resonance at low optical power, we measure a Lorentzian profile, and fit it to extract a FWHM linewidth of 55.1 MHz. This corresponds to a loaded quality factor of $Q_L = 3.55$ million (Fig. 5(b)). From this, and the transmission of the resonance T, we calculate an intrinsic quality factor of $Q_i = 2Q_L/(1 + \sqrt{T}) = 4.04$ million. This corresponds to a propagation loss of 9 dB/m, which includes bending loss from the racetrack design. Note that our low-loss resonators are created using a single-step ma-N-based lithography process, thereby avoiding an additional dry etching step and complexity associated with a hard-mask transfer, such as that used in Ref. [8].

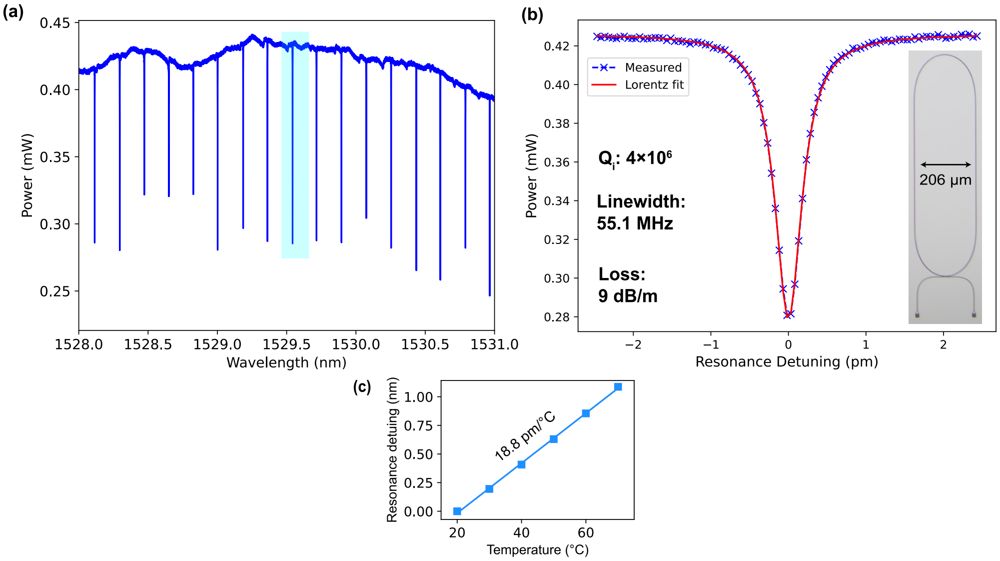

Fig. 5. Optical resonator measurements. (a) Measured optical spectrum of a single-mode TFLT racetrack resonator. The resonance shown in (b) is indicated by the blue shaded area. (b) Measured (x) and fit (red line) Lorentzian-shaped resonance used to determine linewidth, intrinsic quality factor, and loss coefficient indicated. Inset: optical micrograph of the corresponding fabricated racetrack resonator. (c) Measured and fitted temperature-dependent response extracted from the resonance shift of the racetrack resonator as a function of temperature.

As a last step we measure the temperature dependence of the TFLT refractive index. This is performed by temperature tuning the chip similar to that for the eye diagram measurements, and monitoring the detuning of the resonance. The detuning is linear with temperature (Fig. 5(c)). A fit suggests a thermo-optic coefficient of $dn/dT = 3 \times 10^{-6}K^{-1}$, including effects of resonator geometry and thermal expansion of LT only [20]. This differs from $12 \times 10^{-6}K^{-1}$ estimated from bulk LT [20] due to the presence of the material stack, piezoelectricity, film properties, e.g., free charges or crystal structure differences due to etching or wafer cutting and bonding, or a combination of these effects.

8. Conclusion

We demonstrate thin-film lithium tantalate Mach-Zehnder modulators that have improved DC stability, both in timescale and magnitude, over equivalent Mach-Zehnder modulators in thin-film lithium niobate. Importantly, we do not sacrifice key figures-of-merit including RF bandwidth, drive voltage and optical loss, and fabricate the modulators with a scalable process using ma-N resist. Our path-length balanced modulator design mitigates against temperature and laser wavelength fluctuations, which has practical benefits in deployment. Furthermore, low-error data modulation at varied temperature and optical powers is also shown. Our fabrication process yield low single-mode loss of 9 dB/m. We expect that optimization of charge dynamics near surfaces, either by etching or metallization studies, could further improve the performance of thin-film lithium niobate electro-optics beyond what is presented here. During the preparation and review of this manuscript, two other works [21,22] have reported improved DC stability using TFLT.

Funding. National Science Foundation (EEC-1941583, 2138068); Air Force Office of Scientific Research (FA9550-20-1-01015); National Aeronautics and Space Administration (80NSSC22K0262); Naval Air Warfare Center, Aircraft Division (N6833522C0413); Amazon Web Services.

Acknowledgments. The authors thank D. Renaud, D. Zhu, M. Yeh, D. Barton, and C.J. Xin. This work was performed in part at the Harvard University Center for Nanoscale Systems (CNS); a member of the National Nanotechnology Coordinated Infrastructure Network (NNCI), which is supported by the National Science Foundation under NSF award no. ECCS-2025158.

Disclosures. The authors declare that there are no conflicts of interest related to this article.

Data availability. Data is available upon request.

References

1. D. Zhu, L. Shao, M. Yu, *et al.*, "Integrated photonics on thin-film lithium niobate," Adv. Opt. Photonics **13**(2), 242–352 (2021).
2. X. Zhu, Y. Hu, S. Lu, *et al.*, "Twenty-nine million intrinsic q-factor monolithic microresonators on thin-film lithium niobate," Photonics Res. **12**(8), A63–A68 (2024).
3. M. Xu, M. He, H. Zhang, *et al.*, "High-performance coherent optical modulators based on thin-film lithium niobate platform," Nat. Commun. **11**(1), 3911 (2020).
4. J. Holzgrafe, E. Puma, R. Cheng, *et al.*, "Relaxation of the electro-optic response in thin-film lithium niobate modulators," Opt. Express **32**(3), 3619–3631 (2024).
5. X. Yan, Y. Liu, L. Ge, *et al.*, "High optical damage threshold on-chip lithium tantalate microdisk resonator," Opt. Lett. **45**(15), 4100–4103 (2020).
6. J. Shen, Y. Zhang, C. Feng, *et al.*, "Hybrid lithium tantalite-silicon integrated photonics platform for electro-optic modulation," Opt. Lett. **48**(23), 6176–6179 (2023).
7. J. Yu, Z. Ruan, Y. Xue, *et al.*, "Tunable and stable micro-ring resonator based on thin-film lithium tantalate," APL Photonics **9**(3), 036115 (2024).
8. C. Wang, Z. Li, J. Riemensberger, *et al.*, "Lithium tantalate photonic integrated circuits for volume manufacturing," Nature **629**(8013), 784–790 (2024).
9. J. L. Casson, K. T. Gahagan, D. A. Scrymgeour, *et al.*, "Electro-optic coefficients of lithium tantalate at near-infrared wavelengths," J. Opt. Soc. Am. B **21**(11), 1948–1952 (2004).
10. S. Çabuk and A. Mamedov, "Urbach rule and optical properties of the linbo$_3$ and litao$_3$," J. Opt. A: Pure Appl. Opt. **1**(3), 424–427 (1999).
11. M. Jacob, J. Hartnett, J. Mazierska, *et al.*, "Temperature dependence of permittivity and loss tangent of lithium tantalate at microwave frequencies," IEEE Trans. Microwave Theory Tech. **52**(2), 536–541 (2004).
12. F. Holtmann, J. Imbrock, C. Bäumer, *et al.*, "Photorefractive properties of undoped lithium tantalate crystals for various composition," J. Appl. Phys. **96**(12), 7455–7459 (2004).
13. O. Althoff and E. E. Kraetzig, "Strong light-induced refractive index changes in LiNbO3," in *Nonlinear Optical Materials III*, vol. 1273 P. Guenter, ed., International Society for Optics and Photonics (SPIE, 1990), pp. 12–19.
14. Y. Kong, F. Bo, W. Wang, *et al.*, "Recent progress in lithium niobate: Optical damage, defect simulation, and on-chip devices," Adv. Mater. **32**(3), 1806452 (2020).
15. R.-Y. Yang, Y.-K. Su, M.-H. Weng, *et al.*, "Characteristics of coplanar waveguide on lithium niobate crystals as a microwave substrate," J. Appl. Phys. **101**(1), 014101 (2007).
16. D. B. Maring, R. F. Tavlykaev, R. V. Ramaswamy, *et al.*, "Waveguide instability in litao$_3$," J. Opt. Soc. Am. B **19**(7), 1575–1581 (2002).
17. Y. Yan, K. Huang, H. Zhou, *et al.*, "Wafer-scale fabrication of 42° rotated y-cut litao$_3$-on-insulator (ltoi) substrate for a saw resonator," ACS Appl. Electron. Mater. **1**(8), 1660–1666 (2019).
18. D. Renaud, D. Assumpcao, C. Jin, *et al.*, "Mitigating electron beam induced defects for low-loss and stable active photonic circuits," in *CLEO* (Optica Publishing Group, 2024), paper SF3G.7.
19. P. Kharel, C. Reimer, K. Luke, *et al.*, "Breaking voltage–bandwidth limits in integrated lithium niobate modulators using micro-structured electrodes," Optica **8**(3), 357–363 (2021).
20. G. Ghosh, "Thermo-optic coefficients of linbo 3, liio 3, and litao 3 nonlinear crystals," Opt. Lett. **19**(18), 1391–1393 (1994).
21. H. Wang, X. Xing, Z. Ruan, *et al.*, "Optical switch with an ultralow dc drift based on thin-film lithium tantalate," Opt. Lett. **49**(18), 5019–5022 (2024).
22. C. Wang, D. Fang, A. Kotz, *et al.*, "Ultrabroadband thin-film lithium tantalate modulator for high-speed communications," arXiv (2024).